



Mesophase in melt-spun poly(ϵ -caprolactone) filaments: Structure–mechanical property relationship

F. Selli^{a,b,*}, U.H. Erdoğan^b, R. Hufenus^a, E. Perret^{a,c}

^a Laboratory for Advanced Fibers, Empa, Swiss Federal Laboratories for Materials Science and Technology, Lerchenfeldstrasse 5, 9014, St. Gallen, Switzerland

^b Dokuz Eylül University, Department of Textile Engineering, Buca-Izmir, Turkey

^c Center for X-ray Analytics, Empa, Swiss Federal Laboratories for Materials Science and Technology, Überlandstrasse 129, 8600, Dübendorf, Switzerland

ARTICLE INFO

Keywords:

Poly (ϵ -caprolactone)

Melt-spinning

Mesophase

Biodegradable fiber

WAXD

SAXS

X-ray diffraction

ABSTRACT

Fine poly(ϵ -caprolactone) (PCL) filaments (diameter: 59–92 μm) were successfully melt-spun with modified drawing setups to prevent draw instabilities. Depending on the production parameters, different mechanical properties were obtained (tensile strength: 302–456 MPa, elongation at break: 69–88%). These variations are related to subtle structural differences, which we have analyzed with wide-angle x-ray diffraction (WAXD) and small-angle x-ray scattering (SAXS). SAXS was used to determine crystal widths and the spacing between crystals along the filament axis. Additionally, 2D WAXD patterns were simulated and WAXD profiles were fitted. The detailed 2D WAXD analysis revealed that a highly-oriented non-crystalline mesophase is present in drawn PCL filaments, which is most-likely situated in-between PCL crystals. A large amount of this mesophase (>16%), combined with high crystalline orientation and perfect crystals, led to higher tensile strength values. We also confirmed that PCL chains pack with non-planar chain conformations in the unit cell.

1. Introduction

Poly(ϵ -caprolactone) (PCL) is a synthetic biodegradable aliphatic polyester [1–3] which is biocompatible [4] and has good mechanical properties [5]. The low melting point of PCL ($\sim 60^\circ\text{C}$) and the slow biodegradation rate in the human body (several years) make PCL suitable for biomedical applications like long-term drug delivery or long-lasting implants, sutures and 3D scaffolds for tissue engineering [1, 4, 6–10]. Additionally, PCL is compatible with a wide range of other polymers and thus has been investigated as a polymer blend component or copolymer for various applications [11–15]. PCL in the form of filaments is of particular interest for technical textiles. Despite the growing interest, only a few studies discuss the melt-spinning of PCL homo-component filaments [16–19]. In these studies, thick monofilaments (280–900 μm) were produced, using a spin-drawing process, where filaments were directly melt-spun into a water or ice-water bath and afterwards drawn in different drawing zones.

We have melt-spun PCL monofilaments without the use of a water bath in order to achieve fine filaments in an economic and upscalable way. Stress-induced necking (abrupt decrease in filament cross-sectional area) usually occurs in the drawing process of PCL. If the position of the

necking point is unstable and eventually moves onto a godet, necking can be disturbed, leading to oscillations in the filament tension. Such draw instabilities can finally result in local fluctuations of the monofilament cross-section and in frequent fiber breakage. In order to avoid such instabilities, we have successfully modified the online melt-spinning line as well as an offline drawing setup (experimental section).

So far, most of the previously published studies on melt-spun PCL filaments have focused on investigating the effect of processing parameters on mechanical properties. However, x-ray studies that present structural properties of melt-spun PCL filaments [17] or PCL films [20] are scarce. Two different crystal structures have been proposed for PCL in the past: Chatani et al. have suggested an orthorhombic crystal structure with lattice parameters of $a = 7.47 \text{ \AA}$, $b = 4.98 \text{ \AA}$ and c (molecular chain axis) = 17.05 \AA with two non-planar molecular chains per unit cell [21]. In contrast, Bittiger et al. have proposed that the chains adopt planar chain conformations [22]. Hu et al. [23] have performed electron diffraction measurements and have found that the chains pack with non-planar chain conformations because of the twist near the ester linkage. This finding was in agreement with the previously suggested structure by Chatani et al. [21].

Here, we present a detailed structural analysis of melt-spun PCL

* Corresponding author. Laboratory for Advanced Fibers, Empa, Swiss Federal Laboratories for Materials Science and Technology, Lerchenfeldstrasse 5, 9014, St. Gallen, Switzerland.

E-mail address: figen.selli@ogr.deu.edu.tr (F. Selli).

<https://doi.org/10.1016/j.polymer.2020.122870>

Received 29 April 2020; Received in revised form 10 July 2020; Accepted 28 July 2020

Available online 4 August 2020

0032-3861/© 2020 The Authors.

Published by Elsevier Ltd.

This is an open access article under the CC BY-NC-ND license

(<http://creativecommons.org/licenses/by-nc-nd/4.0/>).

monofilaments (59–92 μm) with wide-angle x-ray diffraction (WAXD) and small-angle x-ray scattering (SAXS). Azimuthal and equatorial profiles of measured 2D WAXD patterns were fitted with extracted profiles from 2D simulated WAXD patterns, based on the theory previously developed by Burger et al. [24]. These 2D fittings were performed to confirm the crystal structure of PCL and to get more precise estimates for crystal widths and preferred orientation than with conventional 1D profile analysis methods. The results of the 2D fitting procedure reveal that there exists a highly-oriented mesophase in PCL, which is most-likely situated in-between PCL crystals. This mesophase leads to a broad asymmetric equatorial reflection that lies underneath the equatorial (110) and (200) reflections. Mechanical and thermal properties of all drawn filaments are correlated with the findings from the structural analysis.

2. Experimental

2.1. Materials

Four PCL monofilaments were melt-spun from the PCL Capa™ 6500 provided by Perstorp (UK) (Prochem AG, Zürich/Switzerland) in the form of pellets. The PCL (density of 1.1 g/cm^3 , nominal mean molecular weight of $M_w = 50$ kDa) had a melt flow index of 5.9–7.9 $\text{g}/10$ min (at 160 $^\circ\text{C}$ and a load of 2.16 kg) and a melting point of $T_m = 58$ –60 $^\circ\text{C}$. Results from rheology, differential scanning calorimetry (DSC) and thermogravimetric (TGA) measurements of the polymer material are summarized in the data in brief article [25]. Rheology measurements have shown that the viscosity of the PCL melt remained stable at elevated temperatures up to 10 min. Also both, the loss and storage modulus, were stable for 30 min and no degradation was observed.

2.2. Melt-spinning, online drawing and offline drawing of PCL filaments

Melt-spinning of PCL monofilaments was carried out on a custom-made pilot-scale melt-spinning plant described elsewhere [26]. In total four filaments were melt-spun, an as-spun (undrawn) filament, I_{UD} , as well as three online drawn filaments (II–IV). Processing parameters for all PCL monofilaments produced are summarized in Table 1. Prior to melt-spinning, the PCL polymer was dried in a vacuum oven at 45 $^\circ\text{C}$ for 12 h. PCL pellets were melted using a 14 mm single screw extruder with a length to diameter (L/D) ratio of 25. Extruder pressure needed for an effective operation of the melt pump was set to 80 bar, and nominal throughput of the gear pump was 3 cm^3/min . Extrusion temperatures were graduated between 60 and 100 $^\circ\text{C}$, which is a few tens of degrees higher than the polymer melting temperature ($T_m = 57.8$ $^\circ\text{C}$ [25]) to achieve a high enough melt-viscosity for processing. While the spin pack temperature was set to 100 $^\circ\text{C}$ for filaments I_{UD} and II, it was decreased to 90 $^\circ\text{C}$ for filaments III and IV, in order to accelerate the cooling of the monofilaments. The circular monofilament die had a diameter of 0.5 mm and a capillary L/D ratio of 4. The polymer melt leaving the spinneret was subsequently cooled down in an air cooling chamber with a height of 1.2 m at 11 $^\circ\text{C}$. All four godet temperatures were set to 30 $^\circ\text{C}$, and the draw ratio (DR), defined as the ratio between speeds of winder and take-up godet, was 6 for all online drawn filaments. DR = 6 was the highest draw ratio that could be achieved for online drawn filaments

without frequent fiber breakage.

The as-spun PCL filament (I_{UD}) was subsequently drawn offline with the custom-made drawing and winding machine SSM RM3-T DIG-ICONE® preciflex™ (Schärer Schweiter Mettler AG, Switzerland). For the resulting filament, I_{DR} , a DR of 7 could be achieved. A heating chamber (set to 50 ± 5 $^\circ\text{C}$) was placed between the first and second godet in order to uniformly heat the filament, enhancing the molecular mobility. In total, three godets were used for offline drawing (Fig. 1). Offline drawn godet speeds (Table 1) were chosen significantly lower compared to online drawing, in order to address the time-dependent viscoplastic behavior and thus enhance mobility and extension of polymer chains.

In both, the online and offline drawing setup, the filaments were directed over an intermediate godet (godet 2) in reverse direction with respect to the rotation of the godet, in order to induce localized friction to the filament. This additional friction promoted the stress-induced necking and thus stabilized the position of the necking point [25]. Note that the filament was drawn over this particular godet without loops. The possibility to fine-tune the speed of godet 2 makes it possible to achieve a stable necking point position and with that a stable drawing process. Note that the processing window for the speed of the godet is quite small, lower or higher speeds lead to draw instabilities. An alternative method for stabilization would be to use a pin, but this method would inflict too much friction onto the fiber when drawing online with high speeds, leading to fiber breakage.

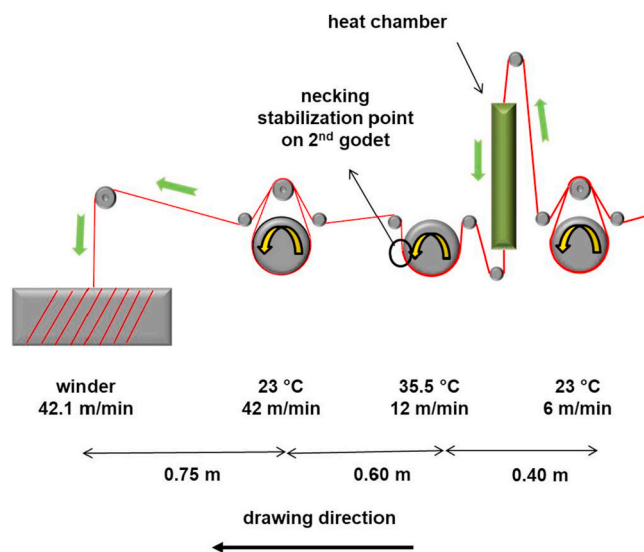


Fig. 1. Schematic assembly of the offline drawing setup. The red color shows the guiding of the filament over and around the godets and separator rolls. (For interpretation of the references to color in this figure legend, the reader is referred to the Web version of this article.)

Table 1

Processing parameters of PCL monofilaments. Number of loops around godets are indicated in brackets.

fiber	spin pack ($^\circ\text{C}$)	spin pressure (bar)	mass throughput (g/min)	godet 1 speed (m/min)	godet 2 speed (m/min)	godet 3 speed (m/min)	godet 4 speed (m/min)	winder speed (m/min)
I_{UD}	100	170	2.06	50	–	–	–	50
I_{DR}	–	–	–	6 (7w)	12 (0w)	42 (3w)	–	42
II	100	120	2.30	50 (8w)	200 (0w)	295 (10w)	300 (6w)	300
III	90	134	2.30	50 (8w)	200 (0w)	295 (10w)	300 (6w)	300
IV	90	134	2.27	100 (8w)	200 (0w)	595 (10w)	600 (6w)	600

2.3. Characterization

2.3.1. Analysis of mechanical properties

An optical microscope (Olympus BX43) was used to analyze the diameter of filaments by averaging over 20 measurements. Mechanical testing of the filaments was performed with the tensile testing machine Statimat ME+ (Textechno, Germany). The load-strain behavior was evaluated with a 100 N load cell in reference to the standard ASTM D 2256 [27]. Filament tests were performed with a gauge length of 50 mm using a constant rate of extension of 100 mm/min. Tensile strength and elongation at break values were obtained by averaging over 10 measurements.

2.3.2. Analysis of thermal properties

Thermal properties of PCL pellets and filaments were characterized using differential scanning calorimetry (DSC) and thermogravimetric analysis (TGA). Measurements with a DSC instrument (DSC 214 Polyma, Netzsch, Selb, Germany) were performed in nitrogen atmosphere (40 mL/min). The following heating and cooling cycles were applied: first heating from 0 °C to 120 °C, followed by a cooling step down to −50 °C and second heating back to 120 °C. The heating and cooling rates were set to 10 °C/min. TGA (TG 209 F1, Netzsch, Selb, Germany) was performed under nitrogen, increasing the temperature from 25 to 600 °C with a heating rate of 10 °C/min.

2.3.3. Analysis of structural properties

WAXD and SAXS patterns were recorded on a Bruker Nanostar U diffractometer (Bruker AXS, Karlsruhe, Germany) with a Cu-K α radiation $\lambda = 1.5419$ Å and a VÅNTEC-2000 MikroGap area detector. WAXD and SAXS measurements were performed several days after melt-spinning for the online drawn fibers and offline-drawn fiber. The as-spun fiber was measured 30 months after melt-spinning. Single filaments were used for all WAXD and SAXS measurements, which were performed in two separate experiments with distances of 19.1 cm and 110.1 cm, respectively, between the sample and the active detector area. The recorded WAXD/SAXS patterns were analyzed with the evaluation software DIFFRAC.EVA (version 4.2., Bruker AXS, Karlsruhe, Germany) and specifically developed python codes.

2.4. WAXD analysis: crystallinity

WAXD patterns were measured in order to determine the crystallinity of the individual PCL filaments. The crystallinity was determined according to the previously described procedure in another publication [28]: The radially integrated profiles were Lorentz corrected and polarization corrected. The amorphous phase was subtracted from the radial profiles and the integrated annuli (110) and (200) were fitted with Pearson VII functions leading to calculated percentages of WAXD intensities (meas. crystallinity) of diffraction spots that are arising from crystal planes.

2.5. WAXD analysis: 2D pattern simulation and fitting procedures

We have simulated 2D WAXD patterns of PCL based on the theory introduced by Burger et al. [24]. The scattered x-ray intensity of an individual (hkl) plane in reciprocal space is directly proportional to the modulus square of the unit cell structure factor. In order to calculate the latter, it is necessary to know the atomic positions of all atoms in the unit cell. For this purpose, we have made a unit cell structure file (.cif) from the structural parameters given by Chatani et al. [21] and have loaded the file into the open-source software 'Mercury' [29] to extract the atomic coordinates x_j , y_j , z_j of all atoms (including hydrogens) in the orthogonal PCL unit cell. We used the orthogonal unit cell vectors \mathbf{a} , \mathbf{b} , \mathbf{c} , to calculate the reciprocal space vectors \mathbf{a}^* , \mathbf{b}^* , \mathbf{c}^* .

The scattering vectors, \mathbf{s}_{hkl} of (hkl) planes represent the nodes in reciprocal space, with $|\mathbf{s}_{hkl}| = 2\sin(\theta_{hkl})/\lambda$.

$$\mathbf{R}_j = x_j\mathbf{a} + y_j\mathbf{b} + z_j\mathbf{c} \quad (1)$$

$$\mathbf{s}_{hkl} = h\mathbf{a}^* + k\mathbf{b}^* + l\mathbf{c}^* \quad (2)$$

The coefficients from the international tables for crystallography [30] were used for the analytical approximation of the atomic form factors f_j [25] in order to calculate the structure factors squared. The isotropic thermal displacement parameters, B , were taken from Chatani et al. [21] for the Debye-Waller factor calculations of the individual atoms in the crystal. The unit cell structure factor squared is thus given by the following equation:

$$|F_{hkl}(\mathbf{s}_{hkl})|^2 = \left| \sum_{j=1}^N f_j \exp(-2\pi i(\mathbf{s}_{hkl} \cdot \mathbf{R}_j)) \exp\left(-B \frac{|\mathbf{s}_{hkl}|^2}{4}\right) \right|^2 \quad (3)$$

The measured WAXD intensity is proportional to the averaged intensity from the (hkl) planes over the spherical surface with radius $|\mathbf{s}_{hkl}|$. The finite crystallite size (crystal width perpendicular to fiber axis), D , leads to a fixed width, $w=1/D$, of the reflections in reciprocal space. We make use of a Lorentzian distribution function to account for the broadening of the peaks due to the finite crystal size. The scattered intensity distribution of a (hkl) plane with polar angle ϕ_{hkl} is given by

$$\overline{I(s, \phi_{hkl})} = \frac{1}{(4\pi w |\mathbf{s}_{hkl}|^2)} I_{hkl}(\mathbf{s}_{hkl}) \frac{1}{1 + [\pi(s - s_{hkl})/w]^2} \quad (4)$$

Since the crystal size depends on the crystalline direction, we have introduced for reflection (110) another fixed width parameter $w_{(110)}$. The scattered intensity $I_{hkl}(\mathbf{s}_{hkl})$, is proportional to the above given unit cell structure factors squared [25]. The Onsager distribution function, $F(\phi, \phi_{hkl})$, takes into account the orientation of the crystallites, where p_0 is the isotropic randomly oriented fraction of crystals in the filament and p' is the azimuthal width of the peaks arising from the oriented crystal fraction.

$$F(\phi, \phi_{hkl}) = p_0 + (1 - p_0) \left(\frac{p' \cosh(p' \cos \phi \cos \phi_{hkl})}{\sinh(p')} \right) I_0(p' \sin \phi \sin \phi_{hkl}) \quad (5)$$

The overall averaged intensity arising from the crystals in the filament is given by

$$\overline{J(s, \phi)} = \overline{I(s, \phi_{hkl})} F(\phi, \phi_{hkl}) \quad (6)$$

A Gaussian ring, I_{ring} , was used to simulate the intensity contribution from the amorphous phase and a damped asymmetric Gaussian profile, I_{pnc} , was used to simulate the intensity contribution from a highly-oriented non-crystalline mesophase, P_{nc} [25]. A similar mesophase has been previously introduced for poly(3-hydroxybutyrate) [28,31].

Reflections with large $|\mathbf{s}_{hkl}|$ are typically attenuated in measured 2D WAXD patterns. This phenomenon can be explained by crystal imperfections, where atomic groups are displaced statistically around their ideal position. Since we assume radial symmetry, we introduce two different average displacements of atomic groups, one in the ab -plane, ΔX_{12} and one along the c -axis, ΔX_3 . Thus, the intensity is corrected for this disorder with an additional Debye-Waller factor, DWF [25].

Finally, the overall intensity distribution of the simulated 2D WAXD patterns is described with the following function:

$$I_{sim}(s, \phi_{hkl}) = I_{ring} + I_{pnc} + \overline{I(s, \phi_{hkl})} F(\phi, \phi_{hkl}) DWF \quad (7)$$

Normalized integrated azimuthal profiles across the (110) and (200) reflections and integrated equatorial profiles were fit with the normalized profiles extracted from simulated 2D WAXD patterns. Profiles were extracted from 2D patterns using the pyFAI python package. The measured profiles were fitted to the simulated profiles by minimizing the fitting error, χ^2 , using a least square method. To calculate the fitting errors, the measured profiles were interpolated to the simulated angular data points. The total mean square fitting error is given by the sum of fitting errors, χ_k^2 , of the equatorial and the two azimuthal profiles:

$$\chi^2 = \sum_{k=1}^3 \chi_k^2 \quad (8)$$

$$\chi_k^2 = \frac{1}{N_k - n} \sum_{i=0}^{N_k-1} \left(I_{k,i}^{\text{meas}} - I_{k,i}^{\text{sim}} \right)^2$$

with N_k being the number of simulated data points in the k th profile and n the number of fitting parameters. For the best fits (model 1), we have used 6 fitting parameters for the crystalline part (p' , p_0 , w , $w_{(110)}$, $\Delta X_{12}^{\text{crystal}}$, $\Delta X_3^{\text{crystal}}$) and 3 for the Gaussian ring (A , μ , σ) and 3 for the non-crystalline highly-oriented mesophase, P_{nc} , (C , a , $\Delta X_3^{P_{nc}}$). In total, this amounts to 12 fitting parameters. The peak position of the mesophase has been taken to be the same as the position of the amorphous ring in order to reduce the number of fitting parameters. Furthermore, it is expected that the positions are similar since the position of the amorphous ring reflects the average spacing between chains in the amorphous phase and the peak position of the mesophase the average spacing between highly oriented chains [32]. The mesophase was simulated with a strongly damped asymmetric Gaussian profile [25], in order to take into account a distribution of lateral spacings, where large spacings are more unlikely to occur due to the tight packing of stretched oriented chains. The fitting was performed with the *lmfit* python package and the differential evolution method. All fitting parameters were allowed to vary within certain bounds. This model 1, led to the best fitting parameters with the lowest χ^2 errors. We have also performed a fit, which takes into account two crystal size contributions and no P_{nc} mesophase (model 2), leading to 13 fitting parameters. In order to prove that the non-crystalline highly-oriented phase is strongly improving the fit, we have also performed fits without the P_{nc} mesophase (model 3), leading to 9 fitting parameters.

2.6. WAXD analysis: degree of crystal orientation

We have determined the degree of orientation of equatorially aligned crystals by using the best fit parameter results for the azimuthal width, p' , of the peaks [33]. The crystalline orientation is defined as [24,34]:

$$f_{(hk0)} = 1 - 3p'^{-1} [\coth(p') - p'^{-1}] \quad (9)$$

If $f_{(hk0)} = 1$ then the $(hk0)$ planes of the crystals are completely aligned parallel to the filament axis. If $f_{(hk0)} = 0$, then the crystals are randomly oriented. Additionally, it is possible to calculate the overall degree of crystalline orientation by taking into account the isotropic unoriented fraction in the filament, p_0 [35].

$$f_{(hk0)}^{\text{tot}} = (1 - p_0) \{ 1 - 3p'^{-1} [\coth(p') - p'^{-1}] \} \quad (10)$$

2.7. SAXS analysis: long-spacing, coherence length and crystal sizes

Small-angle x-ray scattering (SAXS) was used to determine the long-spacing, L_3 , coherence lengths, H , as well as crystal sizes, D . These parameters were calculated by analyzing integrated meridional and transversal areas of the SAXS patterns [25].

3. Results and discussion

3.1. Mechanical properties

Five different PCL filaments were prepared: as-spun (undrawn), I_{UD} , offline drawn (DR 7), I_{DR} , and online drawn (DR 6), II-IV. Take-up and winding speeds were doubled for sample IV, in order to produce a finer filament (doubled draw-down ratio, i.e. ratio between take-up velocity and die exit velocity). Scanning electron microscope (SEM) images indicate that all PCL monofilaments are uniform in diameter and have smooth surfaces [25]. The drawing parameters, fineness of all filaments and mechanical properties are given in Table 2. Tensile strength and elongation at break of the drawn filaments range from 302 to 456 MPa and 69–88%, respectively.

Corresponding stress-strain curves of drawn PCL monofilaments, in comparison with a polyethylene terephthalate (PET) monofilament having a fineness of 6.9 tex, a diameter of 80 μm and a DR of 4.7 (provided by Monosuisse AG, Switzerland), are shown in Fig. 2. Note that PCL can crystallize quite fast during storage at room temperature due to its low glass transition temperature ($T_g \approx -60^\circ\text{C}$) [36]. However, melt-spun filaments consist of lamellar structures which seem to prevent secondary crystallization. Tensile tests of aged filaments confirmed that drawn filaments have similar mechanical properties after 27 months of aging.

Interestingly, the progression of the PCL tensile curves is very similar to the curve from PET, although the PET filament achieves a considerably higher tensile strength of 556 MPa. Chemical composition, bonds, chain slippage, flexibility and extensibility, as well as the amount of crystalline anchoring points and entanglements, determine the mechanical properties of polymer fibers. For example, all PCL monofilaments have higher elongation at break values than the PET

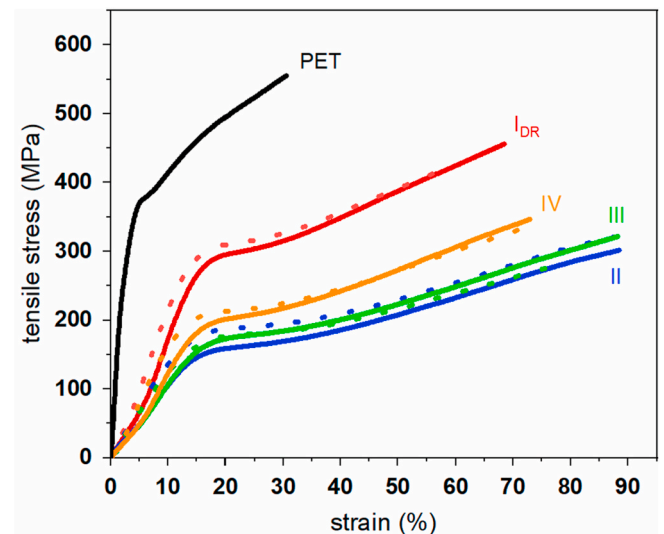


Fig. 2. Tensile stress-strain curves of online (II-IV) and offline drawn PCL filaments (I_{DR}), as well as of a PET monofilament. Measurements of 27 months aged fibers are shown as dashed curves.

Table 2

Drawing parameters, diameter, fineness and mechanical properties of PCL monofilaments. Measurements of filament properties were made one day after production.

fiber	type of drawing	draw ratio DR	diameter (μm)	fineness (tex = mg/m)	specific tensile stress (cN/tex)	ultimate tensile strength (MPa)	elongation at break (%)
I_{UD}	undrawn	1	192.3 ± 1.9	41.2	6.1 ± 0.7	66 ± 8	1224 ± 85
I_{DR}	offline	7	82.1 ± 1.1	6.43	41.5 ± 4.7	456 ± 52	69 ± 13
II	online	6	91.6 ± 0.6	7.65	27.4 ± 1.7	302 ± 19	88 ± 4
III	online	6	92.4 ± 1.3	7.65	29.3 ± 2.1	322 ± 24	88 ± 7
IV	online	6	59.0 ± 0.7	3.79	31.5 ± 1.8	347 ± 20	73 ± 7

monofilament due to the high extensibility of PCL chains.

The highest draw ratio was achieved for the offline drawn PCL, I_{DR} , leading to a high molecular orientation and thus the highest tensile strength (456 MPa) among the PCL filaments produced. The crystalline orientation also increases with increasing draw ratio, which has been confirmed with x-rays (Fig. 4). Interestingly, the offline drawn filament, I_{DR} , has a similar elongation at break as the online drawn filament IV, but has a considerably higher tensile strength, and in consequence a higher toughness [37]. This may be an indication that the smaller speeds and the heating chamber used during offline drawing enable the polymeric chains to better orient, disentangle and form more perfect crystals than during online drawing at high speeds. Such structural differences are elucidated with WAXD and SAXS measurements in section 3.3. Filament, IV, which is the finest filament with a diameter of $\sim 60 \mu\text{m}$, has the highest tensile strength and lowest elongation at break value among the online drawn filaments. We suspect that due to the high take-up speed, a pre-orientation of the chains occurs before take-up, alongside with an elongation of the chains, leading to a stiffening of the filament. Filaments II and III have the smallest tensile strengths and were produced with similar online processing parameters. Structural properties that are responsible for the mechanical properties of all filaments are elucidated in section 3.3. The extracted orientation parameters are summarized in Table 5.

3.2. Thermal properties

PCL is easily crystallizing upon cooling due to a high degree of chain flexibility. Sharp crystallization and melting peaks were observed in the DSC curves for most of the PCL monofilaments (Fig. 3). The broader melting peak of filament II indicates that this filament has a larger crystal size distribution, with crystals that are less perfect than the ones of other filaments. This filament experienced a higher spin pack temperature than filaments III and IV. Thus, crystals may have had more time to grow before strain-induced crystallization started, leading to a larger crystal size distribution with crystals that are less perfect. The melting peaks of filaments I_{DR} and III are sharp, indicating a narrow crystal size distribution with crystals that have a higher degree of perfection.

Thermal properties of PCL monofilaments obtained from DSC curves (1st heating and cooling), including melting temperature T_m , melting enthalpy ΔH_m , crystallization temperature T_c , crystallization enthalpy ΔH_c , and crystallinity X_c , are summarized in Table 3. The crystallinity was estimated from the determined melt enthalpy, ΔH_m , using the following equation [38]:

$$X_c(\%) = \frac{\Delta H_m}{\Delta H_{ref}} \cdot 100 \quad (11)$$

where ΔH_{ref} is the heat enthalpy of an ideal crystal (PCL, 139.5 J/g [38]).

Note that no cold crystallization peak was observed in the second DSC heating cycle, meaning that PCL crystallizes fast upon cooling. First-heating curves (reflect fiber structure) showed that higher crystallinity values were obtained compared to the second heating curves (reflect polymer structure), as explained by the strain-induced crystallization of the filaments during melt-spinning [25].

From Table 3, it can be seen that even the as-spun filament I_{UD} has a high-crystallinity, which is also confirmed by WAXD measurements in section 3.3.1. Most-likely the crystals of this filament have formed during the cool-down in the cooling shaft of the spinneret die and may have grown during the winding or even after the spinning procedure. However, further offline drawing of the filament, I_{DR} , clearly increases the crystallinity even more due to strain-induced crystallization [39].

During online drawing, a first crystallization is most-likely already happening during the first cool-down of the melt in the cooling shaft before the first godet. However, it is difficult to predict how much of the melt already crystallizes before drawing. Further, crystallization occurs during the drawing of the filament due to strain-induced crystallization, which can also be seen by the larger crystallinity, as well as melting and crystallization enthalpy values of online drawn filaments (II-IV) compared to the undrawn filament. Note that PCL can crystallize fast at low temperatures under drawing [40]. After drawing, the filaments are not significantly crystallizing any more, since the lamellar structure prevents a secondary crystallization. We have verified that the filaments have the same structure 27 months after drawing by measuring WAXD of aged fibers [25]. No significant changes in the structure were observed. Even the as-spun fiber retained its structure and after almost 5 years of aging it was still possible to draw the fiber up to 1200% of elongation during a tensile test. This shows that melt-spun PCL fibers do not undergo a significant secondary crystallization at room temperature. Tensile tests of aged filaments also confirmed that drawn filaments have similar properties after 27 months of aging (Fig. 2).

The crystallinity values obtained from DSC are compared to crystallinity values obtained from WAXD measurements in section 3.3.1.

3.3. Structural properties

3.3.1. Wide-angle x-ray diffraction (WAXD) analysis

Fig. 4 shows the measured WAXD patterns of filaments I_{UD} (a) and I_{DR} (b). The sharp intense rings in Fig. 4a indicate that the as-spun filament, I_{UD} , is semi-crystalline and that the PCL crystallites are randomly oriented. Upon drawing, the crystallites orient and sharp diffraction peaks are observed (Fig. 4b). The peaks are indexed to specific lattice planes according to the crystal structure proposed by Chatani et al. [21]. The corresponding unit cell projected along the b -axis is shown in Fig. 4c. The filament axis points along the vertical direction (meridian), whereas the equator is horizontal. The most intense peaks on the equator come from the (110) and the (200) planes with a

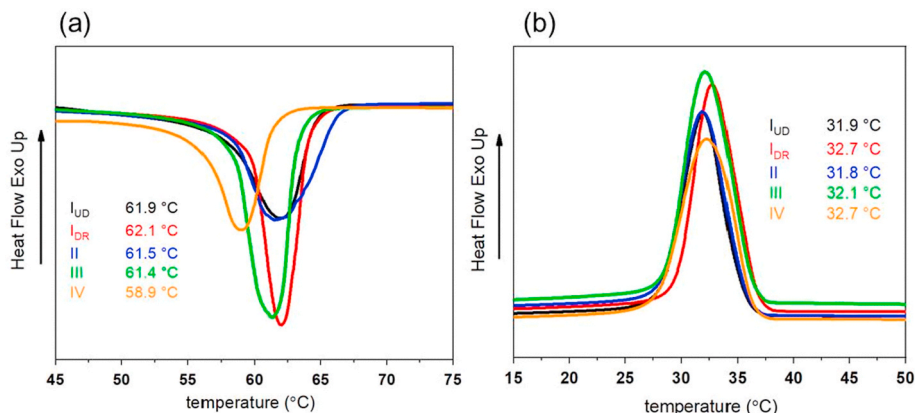


Fig. 3. DSC curves of PCL monofilaments: (a) melting curves, (b) cooling curves of first heating/cooling cycles.

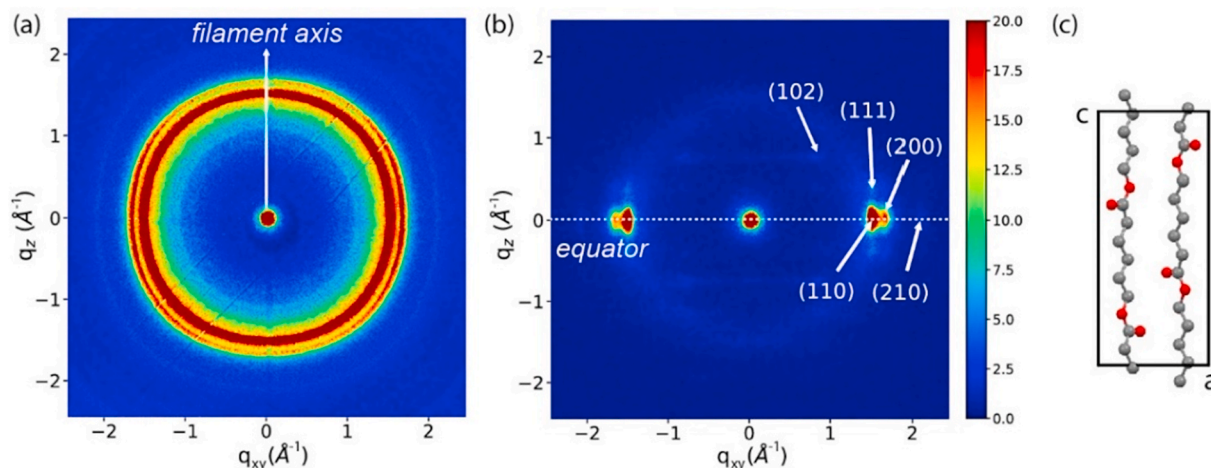


Fig. 4. (a) WAXD pattern of as-spun filament I_{UD} and (b) WAXD pattern of filament I_{DR} , drawn with DR 7. (c) PCL unit cell projected along the b -axis [21].

Table 3

Thermal properties of PCL monofilaments.

fiber	T_m (°C)	ΔH_m (J/g)	T_c (°C)	ΔH_c (J/g)	X_c (%)
I_{UD}	61.9	69.9	31.9	59.3	50.1
I_{DR}	62.1	76.6	32.8	66.7	54.9
II	61.5	78.3	31.9	63.2	56.1
III	61.4	77.2	32.1	68.0	55.3
IV	58.9	72.2	32.8	61.5	51.8

corresponding d -spacing of 4.1 Å and 3.7 Å, respectively.

A summary of all measured WAXD patterns of drawn PCL filaments are given in Fig. 5. At first glance, all WAXD patterns look very alike. However, a detailed 2D analysis reveals that there are subtle differences in e.g. the degree of crystalline orientation and crystallinity.

We have developed python codes in order to simulate 2D WAXD patterns from PCL filaments using the theory from Burger et al. [24,34,41–43]. Measured azimuthal and equatorial profiles were extracted from the two rings across the (110) and (200) reflections and the

equatorial sector as is indicated in the WAXD pattern of the I_{DR} filament in Fig. 5, top left. These measured profiles were subsequently fit with profiles extracted from simulated 2D WAXD patterns. Best fitting errors for all drawn PCL filaments were achieved with model 1, which makes use of the unit cell proposed by Chatani et al. [21] and takes into account an amorphous phase, crystalline phase and a mesophase. An example of a simulated 2D WAXD pattern from best fit parameters for the offline drawn filament, I_{DR} , is shown in Fig. 6. The simulated pattern is well reproducing the main peaks of the measured WAXD pattern.

All fitting errors and the best fit parameters are summarized in the data in brief article, Tables 1 and 2 [25]. Additionally, we have also fitted the WAXD data from filament I_{DR} , using structure factors calculated from the unit cell proposed by Bittiger et al. [22] (model 1a), but the resulting fitting error was almost the double of the best fit error (data in brief article, Table 1 [25]). Thus we conclude that the unit cell structure proposed by Chatani et al. [21] is correct and is well representing the crystal structure of the melt-spun PCL filaments. As mentioned in the theory section, it was necessary to include a mesophase, P_{nc} (highly oriented non-crystalline phase), in the simulated 2D pattern in order to achieve good fits. The P_{nc} gives rise to a rather broad peak on the equator, which lies underneath the (200) and (110) reflection. Such a broad reflection could also arise from small PCL crystals. We have therefore performed a fit which takes into account two crystal size contributions and no P_{nc} mesophase (model 2). However, this fit led to much larger fitting errors, especially for the azimuthal profiles [25], and we therefore exclude that the broad equatorial reflection comes from small crystals. Additionally, we have performed fits where the simulation only included an amorphous phase and a crystalline phase but no P_{nc} mesophase (model 3). Also, these fits led to much larger fitting errors (data in brief article, Table 1 [25]) and thus it can be concluded that a mesophase exists in these PCL filaments. It is suspected that chains from the amorphous phase around and in-between PCL crystals orient and align along the filament axis, leading to this P_{nc} mesophase. We have previously observed a similar mesophase in poly(3-hydroxybutyrate) fibers [28,31], and other authors have also reported mesophases in other polymer materials [44–49]. We suspect that the weak streaks observed on the second layer line are a result of chain slippage along the fiber direction in the mesophase, which we have also seen in previous simulations for poly(3-hydroxybutyrate) [28]. It is suspected that the mesophase, P_{nc} , takes up most of the tensile forces and is uniformly distributing these forces between rigid crystals. Thus not only the crystallinity but also the amount of mesophase can strongly affect the tensile strength of PCL filaments. We have calculated the percentage of the mesophase and amorphous phase, as well as the crystallinity directly from the best fit WAXD patterns, by summing the simulated intensities of the individual phases and dividing them by the

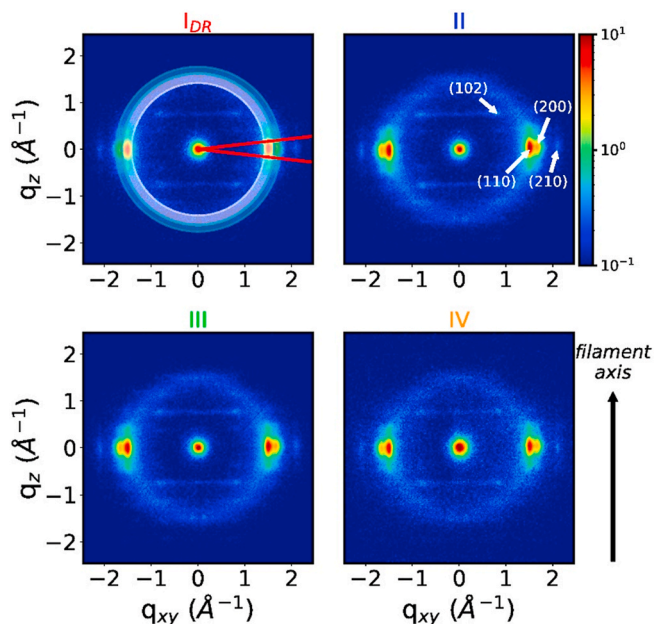


Fig. 5. WAXD patterns of all drawn filaments using a logarithmic scale for the intensities. Azimuthal rings and the equatorial sector are indicated in the top left pattern.

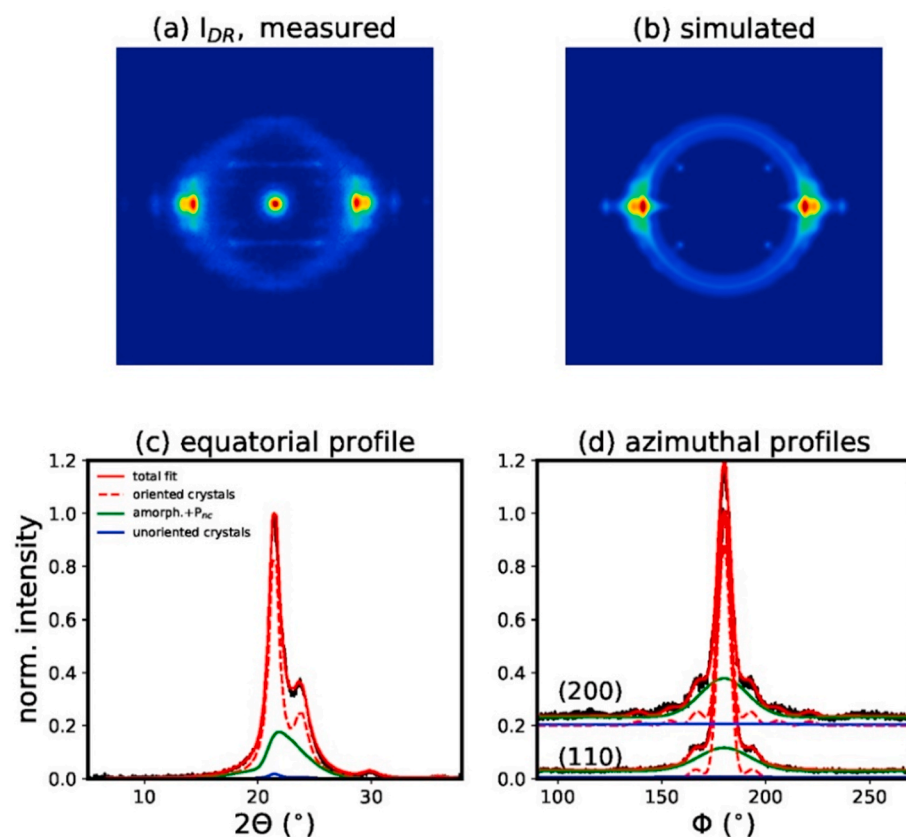


Fig. 6. (a) Measured WAXD pattern of filament I_{DR} . (b) Simulated WAXD pattern using the best fit parameters. (c) Normalized measured equatorial profile (black), best fit (red) and contributions from the oriented crystalline phase (dashed red) and amorphous plus mesophase (green) as well as from randomly oriented crystals (blue) (d) Normalized azimuthal profiles with the same color coding. The azimuthal profile across the (200) reflection is offset for better visibility. The same color coding can be found in the graphical abstract. (For interpretation of the references to color in this figure legend, the reader is referred to the Web version of this article.)

total intensities of the simulated 2D WAXD patterns. A quantification of phases leads to a better understanding of differences in the structures between fibers and thus also the properties. The presented simulation and fitting procedure can be applied to many other polymers as well.

The fitted simulated crystallinity (sim.) is compared to the measured crystallinity (meas.), which was extracted by fitting crystalline peaks in measured radial profiles [25]. Additionally, we compare the values to crystallinities extracted from DSC measurements. All crystallinity values and calculated percentages of the mesophase and amorphous phase are given in Table 4. The obtained crystallinity values from WAXD using the two methods (sim./meas.) described above are quite similar, which confirms that the obtained values are reliable. The crystallinity values obtained from DSC are slightly larger than the ones obtained from WAXD. Note that the measurement technique influences the obtained absolute crystallinity values. For example, WAXD crystallinity values merely reflect the percentage of measured crystalline intensities on the detector screen. However, the obtained values from one method for individual fibers can be compared to one another.

Not only the amount of mesophase and crystallinity are affecting the mechanical properties but also orientation factors of the crystals. As mentioned in the experimental section, we have extracted two orientation parameters. $f_{(hk0)}^{tot}$ takes both, the amount of randomly oriented and highly oriented crystals into account. $f_{(hk0)}$ is the orientation parameter of the highly oriented crystals. In case $f_{(hk0)} = 1$, all highly

oriented crystals have (hk0) planes that are perfectly aligned parallel to the filament axis. The azimuthal width of the reflections, p , is used to calculate the latter preferred orientation of the crystals. The extracted orientation parameters are summarized in Table 5.

The tensile strength of the offline drawn filament, I_{DR} , is the highest, which can be explained by the high mesophase content, high crystallinity and high orientation of crystals. This filament was produced with the largest DR 7, which explains these structural properties. The heating chamber and the low drawing speed in the offline setup made it possible to achieve such a high DR. It is impossible to apply such low speeds in the online drawing setup due to the flow rate of the melted polymer in the cooling shaft. The take-up speed has to be higher than the speed of the gravitational accelerated melt. Also, filament IV has a high tensile strength but has clearly the lowest crystallinity of all filaments. It is

Table 5

Crystal orientation, tensile strength and elongation at break values.

fiber	$f_{(hk0)}^{tot}$	$f_{(hk0)}$	ultimate tensile strength (MPa)	elongation at break (%)
I_{DR}	0.889	0.992	456 ± 52	69 ± 13
II	0.683	0.992	302 ± 19	88 ± 4
III	0.886	0.992	322 ± 24	88 ± 7
IV	0.988	0.991	347 ± 20	73 ± 7

Table 4

Percentages of amorphous phase, mesophase P_{nc} , mesophase plus crystallinity. Crystallinity values extracted from best 2D WAXD fits (sim.) and radial profiles (meas.) of measured WAXD patterns and from DSC measurements.

fiber	amorphous (%)	P_{nc} (%)	$P_{nc} + \text{sim. crystallinity}$ (%)	WAXD sim. crystallinity (%)	WAXD meas. crystallinity (%)	DSC crystallinity, X_c (%)
I_{DR}	36.6	16.1	63.4	47.3	46.4	54.9
II	39.8	12.0	60.2	48.2	47.6	56.1
III	39.2	15.5	60.8	45.3	47.3	55.3
IV	43.4	16.7	56.6	39.9	42.7	51.8

suspected that the faster take-up speed of this filament increases the molecular orientation before drawing, thus reducing the degree of freedom for crystals to develop. Furthermore, the drawn thin filament solidifies faster due to the smaller cross-section and the higher specific surface. Interestingly, both filaments, the offline drawn filament I_{DR}, and the online drawn filament IV have the largest amount of mesophase, P_{nc}, in the filaments. The increased take-up speed of filament IV may have caused a better pre-orientation and stretching of molecular chains, leading to a larger amount of mesophase in the sample. Additionally, filament IV has also the best orientation of all crystals. A slightly higher tensile strength was achieved for filament III than for filament II. The only difference in the filament production was the lower spin pack temperature in the case of filament III (Table 1). Although the determined crystallinities of filament II and III are similar, DSC melting curves show that the crystal size distribution in filament II is broader and crystals are less perfect. The imperfection of the crystals is also reflected in the large out-of-plane displacement fitting coefficient, $\Delta X_3 = 2 \text{ \AA}$, which hit the upper boundary limit during the fitting procedure (data in brief article, Table 2 [25]). Additionally, filament II has the lowest mesophase content. The small tensile strength of filament II can therefore be explained by the small amount of mesophase and by imperfect crystallization, which seem to be a result of the higher spin pack temperature. Larger crystals may form before strain-induced crystallization starts, giving the mesophase less room to develop.

As mentioned above, the mesophase is most likely made of tie molecules that are located in-between PCL crystals, and these stretched tie molecules act as load-bearing points. The above observed influence of the mesophase content on the mechanical properties confirms this hypothesis. From the 2D WAXD fit parameters (data in brief article, Table 2 [25]) we can estimate the average spacing between adjacent chains $\Delta d = \lambda/[2 \sin(\mu/2)]$, in the mesophase. The fitted width of the mesophase, σ , reflects the spread of this spacing. Thus, the spacing in-between chains in the mesophase varies between 4 and 4.5 Å, which is slightly larger than the distances between chains, $d_{(200)} = 3.735 \text{ \AA}$, in

the unit cell along the *a*-axis. The asymmetry of the mesophase peak may be a result of the probability of stretched chains to adopt specific spacings.

3.3.2. Small-angle x-ray scattering (SAXS) analysis

Fig. 7 shows the measured SAXS patterns of drawn PCL mono-filaments. In all SAXS patterns, there is an elongated streak (lamellar reflection) above and below the direct beam, which comes from coherently diffracting aligned PCL crystals, as is shown in the schematic at the bottom right of Fig. 7.

The vertical dashed black lines indicate the meridional areas which were integrated and fit to Pearson VII functions [25]. The meridional peak positions, *z*, of the streak-like lamellar reflections are used to calculate the long-spacing, *L*₃, which reflects the average distance between PCL crystals along the filament axis (see schematic in Fig. 7). The widths of the meridional peaks, σ_{mer} , are related to the coherence length, *H*, which reflects the average height of coherently diffracting stacks of PCL crystals along the filament axis. The horizontal dashed white lines indicate the transversal areas, which were also integrated and fit to Pearson VII functions [25]. The average lamellar sizes, *D*, were calculated from the width of the peaks, σ_{tr} , from the transversal profiles, applying the Scherrer equation. The calculated structural parameters (long-spacing, coherence length and crystal sizes) from the SAXS profiles and crystal sizes along specific directions extracted from 2D fits of WAXD patterns are summarized in Table 6. The latter two crystal sizes along specific directions are calculated from the equatorial peak width parameters *w*₍₂₀₀₎ and *w*₍₁₁₀₎ that are obtained from the best fit parameters of WAXD patterns.

The long-spacing, *L*₃, is the largest for the offline drawn filament due to the large DR, thus the crystals are further pulled apart during the drawing than in the online drawing setup. The coherence lengths, *H*, and long-spacings, *L*₃, of the crystals along the filament axis are significantly larger than the crystal sizes perpendicular to the filament axis. This is an indication that the crystals are larger along the filament axis than

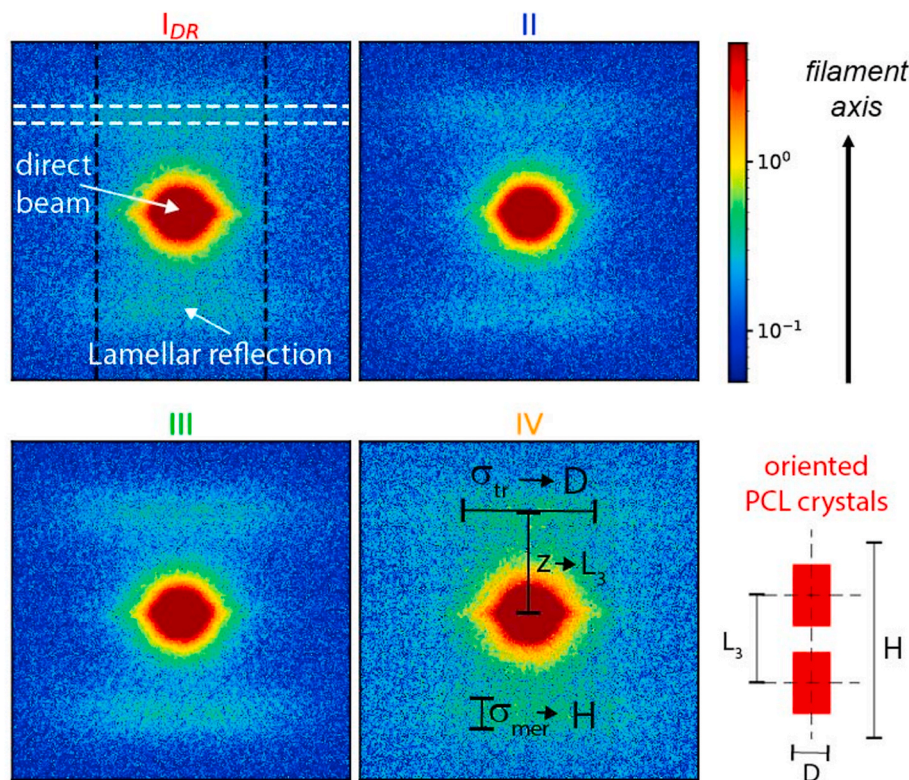


Fig. 7. SAXS patterns of drawn filaments (I_{DR}, II, III, IV). Transversal areas (between dashed white horizontal lines) and meridional areas (between dashed black vertical lines). Bottom right: Schematic of a stack of PCL crystals.

Table 6

Draw ratio, structural parameters of PCL crystals extracted from SAXS patterns and crystal sizes along different directions (D(110), D(200)) extracted from 2D fitting of WAXD patterns.

fiber	draw ratio DR	SAXS L_3 (nm)	SAXS H (nm)	SAXS D (nm)	WAXD $D_{(110)}$ (nm)	WAXD $D_{(200)}$ (nm)
I _{DR}	7	15.5	28.3	6.5	5.8	3.7
II	6	14.7	35.1	6.4	5.8	2.8
III	6	14.8	32.4	6.3	6.0	3.4
IV	6	14.8	30.3	7.7	6.3	3.0

perpendicular to it. The crystal sizes perpendicular to the filament axis, which are extracted from SAXS patterns are larger than the ones extracted from WAXD patterns since the value of D reflects an overall average of all equatorially aligned crystals in the filaments. The crystal sizes extracted from the (200) reflection in the WAXD pattern, however, reflect the crystal sizes along the a -axis ($a = 7.47$ Å). Thus the crystals are rather small and are made of about 4–5 unit cells only along the a -axis. From the sizes along the (110) direction, it follows that the crystals are about 6–7 unit cells long along the b -axis ($b = 4.98$ Å).

4. Conclusion

Fine PCL monofilaments (<100 µm) were melt-spun and subsequently drawn online and offline with processes that are applicable to large-scale industrial filament production. We have shown that the extension-thinning behavior (stress-induced necking) of PCL can be controlled by running the filament over a godet in reverse direction in order to impose localized friction. SAXS measurements have revealed that the long-spacing between crystals along the filament axis depends on the draw ratio. PCL crystals are small and only a few unit cells wide perpendicular to the fiber axis. 2D WAXD simulations have revealed that the unit cell structure of PCL, proposed by Chatani et al. [21], is correctly representing the unit cell that is found in our drawn melt-spun PCL filaments. Furthermore, fitting of azimuthal and equatorial WAXD profiles has revealed that the following phases exist in the drawn PCL filaments: amorphous phase, highly-oriented and partially oriented PCL crystals and a non-crystalline highly-oriented mesophase, P_{nc}. A similar mesophase was introduced earlier for melt-spun poly(3-hydroxybutyrate) fibers [28,31]. The P_{nc} mesophase is most-likely situated between PCL crystals and is made of load-bearing highly-oriented stretched tie-molecules. PCL filaments with high tensile strength (456 MPa, offline drawn filament), have a large mesophase content (>16%) and crystals that are well oriented. Low-speed offline drawing gives the molecular chains more time to disentangle, orient and form more perfect crystals, and thus also higher draw ratios can be achieved. Crystallinity, a narrow crystal size distribution, crystal perfection and orientation of crystals, as well as mesophase content, are all important factors that influence the mechanical properties of polymer fibers. The presented simulation and fitting procedures of 2D WAXD patterns are ideal tools to extract detailed information (e.g. quantification of phases) about the structure of polymer fibers, which would otherwise be missed. A quantification of phases leads to a better understanding of the structures and thus also the properties. The presented simulation and fitting procedure can be applied to other polymers as well. Mesophases may exist in many melt-spun polymer fibers influencing their properties and should be further investigated.

CRediT authorship contribution statement

F. Selli: Investigation, Validation, Visualization, Writing - original draft, Writing - review & editing. **U.H. Erdogan:** Writing - review & editing. **R. Hufenus:** Project administration, Writing - review & editing. **E. Perret:** Supervision, Investigation, Data curation, Writing - original draft, Writing - review & editing.

Declaration of competing interest

The authors declare that they have no known competing financial interests or personal relationships that could have appeared to influence the work reported in this paper.

Acknowledgements

The work was supported by The Scientific and Technological Research Council of Turkey (TÜBİTAK 2214A to Figen Selli). Authors would like to thank Benno Wüst for operating the spinning plant and Markus Hilber for operating the SSM winding machine. We also thank Burger et al. for providing us with basic Mathematica codes, which we have translated into python and further developed for our purposes. We thank A. Gooneie for helping with rheology measurements and analysis.

References

- [1] B. Azimi, et al., Poly (ε-caprolactone) fiber: an overview, *Journal of Engineered Fibers and Fabrics* 9 (3) (2014) 74–90.
- [2] R. Chandra, R. Rustgi, Biodegradable polymers, *Prog. Polym. Sci.* 23 (7) (1998) 1273–1335.
- [3] D. Goldberg, A review of the biodegradability and utility of poly(caprolactone), *J. Environ. Polym. Degrad.* 3 (2) (1995) 61–67.
- [4] M.A. Woodruff, D.W. Hutmacher, The return of a forgotten polymer—polycaprolactone in the 21st century, *Prog. Polym. Sci.* 35 (10) (2010) 1217–1256.
- [5] Y. Zhao, D. Keroack, R. Prud'homme, Crystallization under strain and resultant orientation of poly(ε-caprolactone) in miscible blends, *Macromolecules* 32 (4) (1999) 1218–1225.
- [6] D.W. Hutmacher, et al., Mechanical properties and cell cultural response of polycaprolactone scaffolds designed and fabricated via fused deposition modeling, *J. Biomed. Mater. Res.* 55 (2) (2001) 203–216.
- [7] J.C. Middleton, A.J. Tipton, Synthetic biodegradable polymers as orthopedic devices, *Biomaterials* 21 (23) (2000) 2335–2346.
- [8] C.G. Pitt, *Biodegradable Polymers as Drug Delivery Systems*, Marcel Dekker, New York, 1990.
- [9] M.R. Williamson, A.G.A. Coombes, Gravity spinning of polycaprolactone fibres for applications in tissue engineering, *Biomaterials* 25 (3) (2004) 459–465.
- [10] G. Perale, et al., Lidocaine release from polycaprolactone threads, *J. Appl. Polym. Sci.* 117 (6) (2010) 3610–3614.
- [11] P. Douglas, et al., Analysis of in vitro drug dissolution from PCL melt extrusion, *Chem. Eng. J.* 164 (2) (2010) 359–370.
- [12] B. Gupta, Geeta, A.R. Ray, Preparation of poly(ε-caprolactone)/poly(ε-caprolactone-co-lactide) (PCL/PLCL) blend filament by melt spinning, *J. Appl. Polym. Sci.* 123 (2012) 1944–1950.
- [13] C. Hinuber, et al., Hollow fibers made from a poly(3-hydroxybutyrate)/poly-ε-caprolactone blend, *Express Polym. Lett.* 5 (7) (2011) 643–652.
- [14] Q. Meng, J. Hu, Study on poly(ε-caprolactone)-based shape memory copolymer fiber prepared by bulk polymerization and melt spinning, *Polym. Adv. Technol.* 19 (2) (2008) 131–136.
- [15] J. Pal, et al., Control on molecular weight reduction of poly(ε-caprolactone) during melt spinning — a way to produce high strength biodegradable fibers, *Mater. Sci. Eng. C* 33 (7) (2013) 4213–4220.
- [16] M. Mochizuki, et al., Studies on biodegradable poly(hexano-6-lactone) fibers. Part 2: environmental degradation, in: *Pure and Applied Chemistry*, 1999, p. 2177.
- [17] M. Mochizuki, et al., Studies on the biodegradable poly(hexano-6-lactone) fibers 1. Structure and properties of drawn poly(hexano-6-lactone) fibers (Technical Report), in: *Pure and Applied Chemistry*, 1997, p. 2567.
- [18] A. Charuchinda, et al., Factors influencing the small-scale melt spinning of poly(ε-caprolactone) monofilament fibres 52 (7) (2003) 1175–1181.
- [19] K. Krishnanand, B.L. Deopura, B. Gupta, Determination of intrinsic birefringence values of polycaprolactone filaments, *Polym. Int.* 62 (1) (2013) 49–53.
- [20] T. Kamal, T.J. Shin, S.-Y. Park, Uniaxial tensile deformation of poly(ε-caprolactone) studied with SAXS and WAXS techniques using synchrotron radiation, *Macromolecules* 45 (21) (2012) 8752–8759.
- [21] Y. Chatani, et al., Structural studies of polyesters. III. Crystal structure of poly-ε-caprolactone, *Polym. J.* 1 (1970) 555.
- [22] H. Bittiger, R.H. Marchessault, W.D. Niegisch, Crystal structure of poly-ε-caprolactone, *Acta Crystallogr. B* 26 (12) (1970) 1923–1927.
- [23] H. Hu, D.L. Dorset, Crystal structure of poly(ε-caprolactone), *Macromolecules* 23 (21) (1990) 4604–4607.
- [24] C. Burger, B.S. Hsiao, B. Chu, Preferred orientation in polymer fiber scattering, *Polym. Rev.* 50 (1) (2010) 91–111.
- [25] F. Selli, et al., *Properties, X-Ray Data and 2D WAXD Fitting Procedures of Melt-Spun Poly(ε-caprolactone)* Data in Brief, 2020 (under review).
- [26] R. Hufenus, et al., Biodegradable bicomponent fibers from renewable sources: melt-spinning of poly(lactic acid) and poly[(3-hydroxybutyrate)-co-(3-hydroxyvalerate)], *Macromol. Mater. Eng.* 297 (1) (2012) 75–84.
- [27] ASTM, Standard Test Method for Tensile Properties of Yarns by the Single-Strand Method, 2015.

- [28] E. Perret, et al., Tensile study of melt-spun poly(3-hydroxybutyrate) P3HB fibers: reversible transformation of a highly oriented phase, *Polymer* 180 (2019) 121668.
- [29] C.F. Macrae, et al., Mercury 4.0: from visualization to analysis, design and prediction, *J. Appl. Cryst.* (2020) 53.
- [30] P.J. Brown, et al., Intensity of diffracted intensities, in: E. Prince (Ed.), *International Tables for Crystallography Volume C: Mathematical, Physical and Chemical Tables*, Springer Netherlands, Dordrecht, 2004, pp. 554–595.
- [31] E. Perret, et al., Structural response of melt-spun poly(3-hydroxybutyrate) fibers to stress and temperature, *Polymer* 197 (2020) 122503.
- [32] J. Shimizu, N. Okui, T. Kikutani, Fine structure and physical properties of fibers melt-spun at high speeds from various polymers, in: A. Ziabicki, H. Kawai (Eds.), *High-speed Fiber Spinning*, John Wiley & Sons, New York, 1985, pp. 429–483.
- [33] J.J. Hermans, et al., Quantitative evaluation of orientation in cellulose fibres from the X-ray fibre diagram, *Recueil Des Travaux Chimiques Des Pays-Bas-Journal of the Royal Netherlands Chemical Society* 65 (7–8) (1946) 427–447.
- [34] C. Burger, et al., Small-angle X-ray scattering study of intramuscular fish bone: collagen fibril superstructure determined from equidistant meridional reflections, *J. Appl. Crystallogr.* 41 (2) (2008) 252–261.
- [35] S. Toki, et al., Strain-induced crystallites and temperature-induced crystallites in poly-isoprene by 2D WAXD simulating analysis, in: *Constitutive Models for Rubber VIII - Proceedings of the 8th European Conference on Constitutive Models for Rubbers*, Ecomr, 2013.
- [36] A. Charuchinda, et al., Factors influencing the small-scale melt spinning of poly(ϵ -caprolactone) monofilament fibres, *Polym. Int.* 52 (7) (2003) 1175–1181.
- [37] K. Saigusa, W. Takarada, T. Kikutani, Improvement of the mechanical properties of poly(glycolic acid) fibers through control of molecular entanglements in the melt spinning process, *J. Macromol. Sci., Part B* 59 (6) (2020) 399–414.
- [38] J. Pal, et al., Control on molecular weight reduction of poly(ϵ -caprolactone) during melt spinning—a way to produce high strength biodegradable fibers, *Mater Sci Eng C Mater Biol Appl* 33 (7) (2013) 4213–4220.
- [39] J. Militky, The chemistry, manufacture and tensile behaviour of polyester fibers, in: A.R. Bunsell (Ed.), *Handbook of Tensile Properties of Textile and Technical Fibres*, Woodhead Publishing, 2009, pp. 223–314.
- [40] I. Kelnar, et al., Facile preparation of biocompatible poly (lactic acid)-reinforced poly(ϵ -caprolactone) fibers via graphite nanoplatelets -aided melt spinning, *J Mech Behav Biomed Mater* 84 (2018) 108–115.
- [41] C. Burger, B. Hsiao, B. Chu, X-ray scattering, in: *Polymer Science: A Comprehensive Reference - Volume 2: Polymer Characterization*, Elsevier B.V., 2012, pp. 363–380.
- [42] Y. Mao, et al., Time-resolved synchrotron X-ray scattering study on propylene-1-butylene random copolymer subjected to uniaxial stretching at high temperatures, *Macromolecules* 45 (2) (2012) 951–961.
- [43] Y. Mao, et al., Wide-angle X-ray scattering study on shear-induced crystallization of propylene-1-butylene random copolymer: experiment and diffraction pattern simulation, *Macromolecules* 44 (3) (2011) 558–565.
- [44] L. Luo, et al., Pre-drawing induced evolution of phase, microstructure and property in para-aramid fibres containing benzimidazole moiety, *RSC Adv.* 6 (67) (2016) 62695–62704.
- [45] S. Ran, et al., Structural changes during deformation of Kevlar fibers via on-line synchrotron SAXS/WAXD techniques, *Polymer* 42 (4) (2001) 1601–1612.
- [46] S. Ran, et al., Structural and morphological studies of isotactic polypropylene fibers during heat/draw deformation by in-situ synchrotron SAXS/WAXD, *Macromolecules* 34 (8) (2001) 2569–2578.
- [47] S.F. Ran, et al., Mesophase as the precursor for strain-induced crystallization in amorphous poly(ethylene terephthalate) film, *Macromolecules* 35 (27) (2002) 10102–10107.
- [48] S.F. Ran, et al., Structural and morphological studies of isotactic polypropylene fibers during heat/draw deformation by in-situ synchrotron SAXS/WAXD, *Macromolecules* 34 (8) (2001) 2569–2578.
- [49] F. Auriemma, C. De Rosa, P. Corradini, Solid mesophases in semicrystalline polymers: structural analysis by Diffraction Techniques, in: G. Allegra (Ed.), *Interphases and Mesophases in Polymer Crystallization II*, Springer Berlin Heidelberg, Berlin, Heidelberg, 2005, pp. 1–74.